Role of NH$_3$ binding energy in the early evolution of protostellar cores

S. Kakkenpara Suresh[1,2], O. Sipilä[2], P. Caselli[2], and F. Dulieu[1]

[1] Centre for Astrochemical Studies, Max Planck Institute for Extraterrestrial Physics, Giessenbachstraße 1, 85748 Garching, Germany
e-mail: `shreyaks@mpe.mpg.de`

[2] LERMA, CY Cergy Paris Université, Observatoire de Paris, PSL University, Sorbonne Université, CNRS, LERMA, F-95000 Cergy, France

ABSTRACT

Context. NH$_3$(ammonia) plays a critical role in the chemistry of star and planet formation, yet uncertainties in its binding energy (BE) values complicate accurate estimates of its abundances. Recent research suggests a multi-binding energy approach, challenging the previous single-value notion.
Aims. In this work, we use different values of NH$_3$ binding energy to examine its effects on the NH$_3$ abundances and, consequently, in the early evolution of protostellar cores.
Methods. Using a gas-grain chemical network, we systematically vary the values of NH$_3$ binding energies in a model Class 0 protostellar core and study the effects of these binding energies on the NH$_3$ abundances.
Results. Our simulations indicate that abundance profiles of NH$_3$ are highly sensitive to the binding energy used, particularly in the warmer inner regions of the core. Higher binding energies lead to lower gas-phase NH$_3$ abundances, while lower values of binding energy have the opposite effect. Furthermore, this BE-dependent abundance variation of NH$_3$ significantly affects the formation pathways and abundances of key species such as HNC, HCN, and CN. Our tests also reveal that the size variation of the emitting region due to binding energy becomes discernible only with beam sizes of 10 arcsec or less.
Conclusions. These findings underscore the importance of considering a range of binding energies in astrochemical models and highlight the need for higher resolution observations to better understand the subtleties of molecular cloud chemistry and star formation processes.

Key words. Astrochemistry – ISM: molecules – Radiative transfer – ISM: abundances – Stars: protostars

1. Introduction

Since its detection (Cheung et al. 1968), NH$_3$ has been ubiquitously observed in a variety of environments like molecular clouds (Irvine et al. 1987), prestellar cores (Crapsi et al. 2007), the galactic centre (Winnewisser et al. 1979), diffuse clouds (Liszt et al. 2006), galaxies (Sandqvist et al. 2017; Gorski et al. 2018), star-forming regions (Fehér et al. 2022), comets (Poch et al. 2020), and planet-forming disks (Salinas et al. 2016). It is one of the six major molecules found in interstellar ices in the solid form (Boogert et al. 2015a). It serves as an important tracer in the interiors of dense, starless cores where common tracers like CO and CS are depleted from the gas phase onto dust grains (Caselli et al. 1999; Tafalla et al. 2002) due to temperatures as low as ~ 6K (Crapsi et al. 2007; Pagani et al. 2007) and number densities between 10^4 and 10^6 cm^{-3} (Keto & Caselli 2010). Although NH$_3$ is affected by freeze-out (Caselli et al. 2022), NH$_3$ is selectively tracing dense material, as it is not abundant in the molecular cloud surrounding dense cores (unlike CO and CS).

An important parameter that influences the grain surface abundance of NH$_3$ (and other species) is the binding energy. It serves as a measure of the strength of the interaction between the species and an adsorbate or grain surface. Additionally, once the species is adsorbed onto dust grains, the binding energy plays a crucial role in governing both its diffusion across and residence time on the grain surface. These factors, in turn, significantly influence the physical and chemical conditions governing the evolution of star-forming regions. For example, in the vicinity of a low-mass protostar, the binding energy determines the distance from the central protostar at which sublimation fronts emerge due to the desorption of volatile species from ice grain surfaces. Furthermore, the location of these sublimation fronts, also known as "snowlines" in protoplanetary disks, directly shapes the composition of the planets forming within protoplanetary disks. Hence, precise knowledge of the binding energies is critical for an accurate interpretation of observational data and reliable prediction of abundances through simulations.

Earlier studies, such as Hama & Watanabe (2013), Penteado et al. (2017) and Wakelam et al. (2017), provided a singular binding energy value for NH$_3$ on different types of water ice. However, recent research has challenged this notion, suggesting that NH$_3$ exhibits a distribution of binding energies. Experiments conducted by He et al. (2016) revealed a surface coverage-dependent distribution of binding energies for NH$_3$ at sub-monolayer coverages. Additionally, Kakkenpara Suresh et al. (2024) observed a distribution of binding energies on crystalline ice (3780K – 4080K) and compact amorphous solid water ice (3630K – 5280K) at monolayer coverages. Theoretical calculations by Ferrero et al. (2020), Tinacci et al. (2022), and Germain et al. (2022) have also supported this conclusion. The notion of a binding energy distribution is logical given that the

structure of ice on dust grains is amorphous, resulting in the formation of diverse and unique adsorption sites. This idea is further substantiated by Bovolenta et al. (2020), who obtained a Gaussian-like distribution of binding energies for hydrogen fluoride on amorphous solid water (ASW).

In their numerical study, Grassi et al. (2020) have illustrated that employing a binding energy distribution allows molecules to occupy higher energy binding sites, thereby increasing their residence time on the grain surface. This prolonged residence time enhances their availability to react with other molecules, even at dust temperatures that conventionally exhibit limited or no reactivity. Building upon their findings and our previous work in Kakkenpara Suresh et al. (2024), the present study evaluates the influence of incorporating a range of binding energy values for NH_3 in astrochemical models, in particular the impact of binding energy on the abundance distribution of NH_3. We also investigate the possible effect that NH_3 abundance variations may have on the distributions of other molecules chemically linked to NH_3. We do not expect the measured values of binding energy to have an impact on the chemistry in prestellar cores due to their low temperatures. Hence, in the present work, we focus our attention on protostellar cores. We focus on the very early stages of the evolution of a protostellar core, and use a model of the well-studied class 0 protostellar core, IRAS 16293-2422, as a template for our simulations.

This work is organised in the following way. In Section 2, we outline the physical and chemical model of the protostellar core used. Section 3 presents our results, and Section 4 delves into the implications of these findings along with potential avenues for future research. A concise summary of our work is provided in Section 5.

2. Model

2.1. Physical Model

The core is characterized using the model by Crimier et al. (2010) (Fig. 1) where the radial density profile follows as $n(H_2) \propto r^{-1.8}$ within 6900 AU from the centre, where $n(H_2)$ is the H_2 number density. The source exhibits a pronounced temperature and density gradient. In this model, the temperature of the gas rises significantly towards the interior due to both gas compression during collapse and radiation emitted by the protostar. We assume that the dust temperature and the gas kinetic temperature are equivalent. The analytical approach involves dividing the core into concentric shells, and the final results are combined radially. A two-phase (gas + ice) chemical model with a dust grain radius = 0.1 μm is employed, where the entire ice layer covering the grain is available for desorption.

The abundance profiles are obtained in two steps. First, the initial conditions corresponding to the parent cloud are obtained by running a single-point simulation with $T_{dust} = T_{gas}$ = 10K, $n(H_2) = 10^4$ cm^{-3}, grain radius = 0.1μm, cosmic-ray ionization rate, $\zeta = 1.3 \times e^{-17}$ s^{-1}, and visual extinction A$_V$ = 10 mag. Adsorption, desorption, and photodesorption are also considered, and the simulation is allowed to proceed until a time, t = 10^6 years, consistent with the previous work of Brünken et al. (2014) and Harju et al. (2017) on the source. At this stage, the abundances of all the species are extracted. These are then used as the initial abundances to trace the evolution of the protostellar core. Finally, the abundances of this core
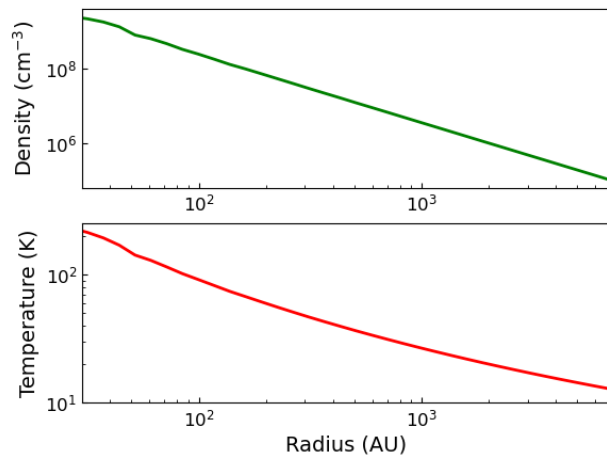
Fig. 1: (Top) The H_2 number density and (bottom) the temperature distribution assumed to model IRAS 16293-2422.

are extracted after an evolutionary time of t = 10^4 years. The choice of time is arbitrary; sub-structure (e.g., a protostellar disk) is expected to form within the inner regions in a timescale of 10^4 - 10^5 years which is not taken into account by the present static physical model. Hence, we chose an early time step (10^4 years) to obtain the abundances, giving an estimate of the initial chemical conditions of the forming small-scale structures.

2.2. Chemical Model

The chemical evolution of the core is monitored by the gas-grain chemical code, *pyRate*, discussed in Sipilä (2012); Sipilä et al. (2010). The model is pseudo-time dependent, i.e., we track the chemical evolution assuming a static core. *pyRate* employs the rate equation method for computing the molecular abundances. The gas-phase network is constructed based on the kida.uva.2014[1] network (Wakelam et al. 2015) with modifications to incorporate deuterated species and spin state chemistry (Sipilä et al. 2015a,b). Here we employ a large chemical network that contains a combined total of over 75,000 reactions in the gas phase and on grain surfaces, with which we simulate the chemistry of NH_3 and its deuterated forms. In addition, the KIDA network is also used to study the effect of proton transfer reactions on the abundances of NH_3 (Section 4.2).

Initially, the species are assumed to be atomic, except for H_2 and HD, and the initial ortho/para H_2 ratio is set to 10^{-3} consistent with a spin temperature, $T_{spin} \sim$ 20K (Brünken et al. 2014; Crabtree et al. 2011). Choosing this specific value for the ratio of ortho/para H_2 corresponds to the assumption that the spin-state ratio has had the time to undergo thermalization prior to the formation of the core. The initial abundances of the species are provided in Table 1. The binding energies for NH_3 on water ice surfaces are sourced from Kakkenpara Suresh et al. (2024). Binding energies of various other species on water ice are obtained from Garrod & Herbst (2006) and Sipilä (2012). The simulated abundances of NH_3 represent the combined

---

[1] https://kida.astrochem-tools.org/networks.html

abundances of the ortho and para forms of the molecule.

Species	Abundance
H_2	5.00×10^{-1}
He	9.00×10^{-2}
HD	1.60×10^{-5}
C^+	1.20×10^{-4}
N	7.60×10^{-5}
O	2.56×10^{-4}
S^+	8.00×10^{-8}
Si^+	8.00×10^{-9}
Na^+	2.00×10^{-9}
Mg^+	7.00×10^{-9}
Fe^+	3.00×10^{-9}
P^+	2.00×10^{-10}
Cl^+	1.00×10^{-9}

Table 1: Initial chemical abundances with respect to total H nuclei, n_H

Fig. 2: Radial abundances of NH_3 in gas phase *(solid lines)* and on grain surfaces *(dashed lines)* at 10^4 years. The binding energies of NH_3 used in each model (colours) are displayed in the lower right corner.

3. Results

3.1. Abundance Profiles

Motivated by the experimental results of Kakkenpara Suresh et al. (2024), we investigated how variations in NH_3 binding energy impact the chemical composition of a protostellar core. For this purpose, we conducted a series of simulations where we systematically varied only the binding energy of NH_3 in each model and traced the resulting chemical evolution with time within the core. We extracted the abundances of NH_3 at t = 10^4 years representing the protostar at its early stages of formation.

Figure 2 presents the abundances of NH_3 at this time in the gas-phase (solid lines) and on grain surfaces (dashed lines) with respect to the radial distance from the centre to the outer edges of the core. The gas-phase abundance of NH_3 decreases moving radially inwards toward the centre of the core before increasing rapidly by several orders of magnitude. The abundance profile shows clear differentiation based on the value of binding energy employed. The region of high NH_3 gas-phase abundance appears closer to the centre with the radius of the desorption zone varying between 150 and 300 AU with increasing binding energy value used. Investigation of the reaction rates at this time step revealed that the primary contributor influencing NH_3 gas-phase abundances is thermal desorption from dust grains. As the binding energy increases, NH_3 remains on the grains until a higher temperature is reached at which point it acquires sufficient thermal energy for desorption.

Notable related effects are only seen in species like HNC, CN, HCN etc (Fig. 3). We find that their abundance profiles vary within the same spatial zone where NH_3 abundances vary. The effects are directly tied via chemical reactions to the variations in the NH_3 abundances. This effect is further discussed in section 4.1. Furthermore, we analyzed the relative abundances of key volatile compounds found in ices, namely NH_3, CO, CO_2, CH_4, and CH_3OH with respect to H_2O. We compared our predictions with the reported values in Boogert et al. (2015b), but direct comparisons are challenging due to
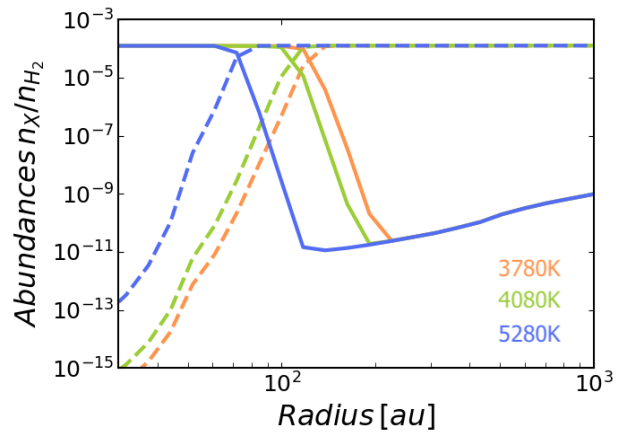
differences in the sources and uncertainties related to the parameters employed for calculating ice abundances in the cited study. Further details of these comparisons are available in appendix A.

3.2. Column Density maps of p-NH_3

To assess the potential observational impact of the NH_3 abundance variations, we have simulated NH_3 column density maps individually for each BE value. Here we consider p-NH_3 only so that we can compare the column density maps against the simulated emission of the (1,1) transition of this molecule (see Sect. 3.3). To generate the column density maps, we employ the radial abundances of p-NH_3 obtained in the previous section as input, which are then interpolated to create a two-dimensional map of the cloud core. The abundances are convolved to a beam size of 2" for the object situated at 120 pc to simulate interferometric observations (the distance to IRAS 16293-2422, although this can be applied to other similar sources by simply changing the distance value). The radial distribution of column density, denoted as *N*, is calculated using the formula:

$$N = \sum_i p \times X_i \times n(H_2)$$

Here, Σ represents the summation across *i* elements of the core model, *p* is the path length through an element *i* in cm, X_i is the abundance of the species (here, p-NH_3) in *i* with respect to H_2, and $n(H_2)$ is the volume density of *i* in mol cm^{-3}. Figure 4 shows the 2D maps of column densities of p-NH_3 within a 300 AU radius where the binding energy-dependent variations are apparent. The radius of the desorption zone decreases as the binding energy increases. The column density as displayed in Fig. 4 traces the part of the distribution that could only be observed with specific NH_3 lines, for example, the (1,1) inversion line. The column density maps also indicate the extent of desorbed NH_3 that will be available in the gas phase.

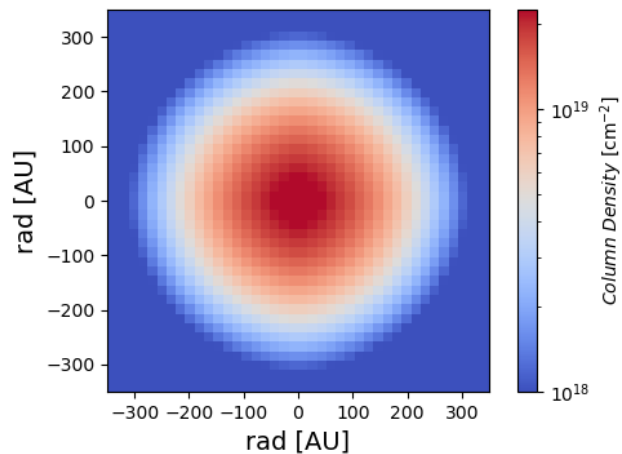### 3.3. Radiative transfer studies of NH_3 (1,1) transition

Subsequently, one-dimensional radiative transfer modelling of the 23 GHz (1,1) rotational-inversion transition of p-NH_3 is carried out to verify the observability of the binding energy-dependent variation in the radius of the desorption zone using
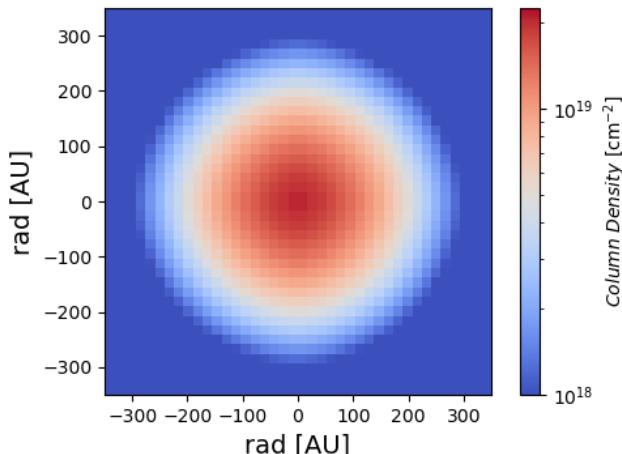
(a)

(a)
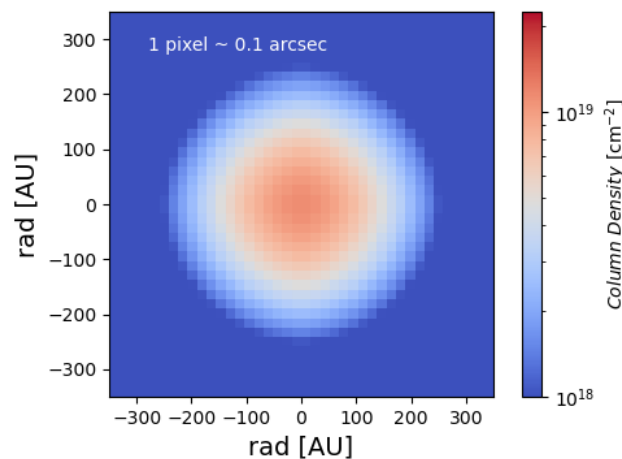

(b)
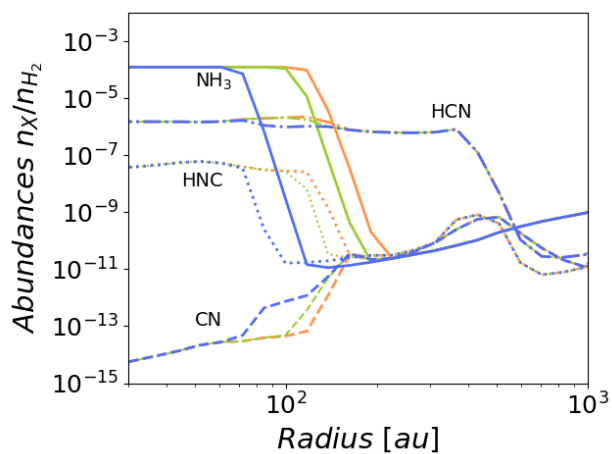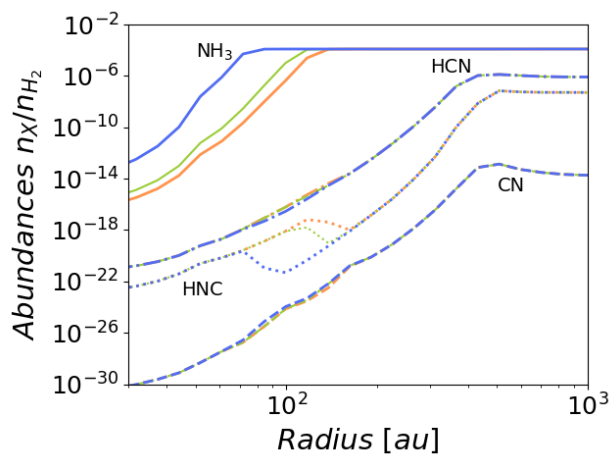
(b)

(c)

Fig. 3: Variation in the (a) gas-phase and (b) grain abundances of NH$_3$, HNC, HCN and CN with binding energy. The colour scheme for the lines follows the same as in Fig. 2

Fig. 4: Column density map of p-NH$_3$ without the envelope (see text) for binding energy (a) 3870K (b) 4080K and (c) 5280K. The angular size simulated by each pixel for each map is given in the top left corner of Fig. 4c.

the non-LTE radiative transfer code LOC (Juvela 2020). The first step in this analysis is to simulate the cloud that contains the protostellar core and its envelope. Given that our source is a Class 0 object, the core represents a deeply embedded source surrounded by an envelope. The methodology employed to determine NH$_3$ abundances within the envelope closely follows the two-step approach outlined for the core in Section 2.1. First, we obtain the abundances corresponding to the parent cloud by running a single-point simulation for t = 10^6 years under the same conditions as the parent cloud, similar to that described in Section 2.1. After extracting the NH$_3$ abundances at this stage, we run a second single-point simulation, this time using the specific physical conditions for the envelope. These conditions include an envelope thickness set to 0.1 pc (5 × 10^{17} cm) assuming a visual extinction, A$_V$, = 5 mag, n(H$_2$) = 10^4 m^{-3} and T = 10 K. The modelling is done taking into consideration the 18 hyperfine components of p-NH$_3$. The velocity resolution is set to ~ 0.835 km/s such that it is high enough to distinguish the hyperfine components. The spectra are obtained for 1000 lines of sight across the radius of the whole object. Each spectrum is then convolved to a synthesized beam of 2". The intensity of the transition from these spectra is integrated and interpolated to create a two-dimensional intensity map (Fig. 5) assuming

spherical symmetry.

The collisional and radiative rate coefficients for the p-NH$_3$ line simulations were taken from the LAMDA database (Schöier et al. 2005). The provided coefficients (collisional
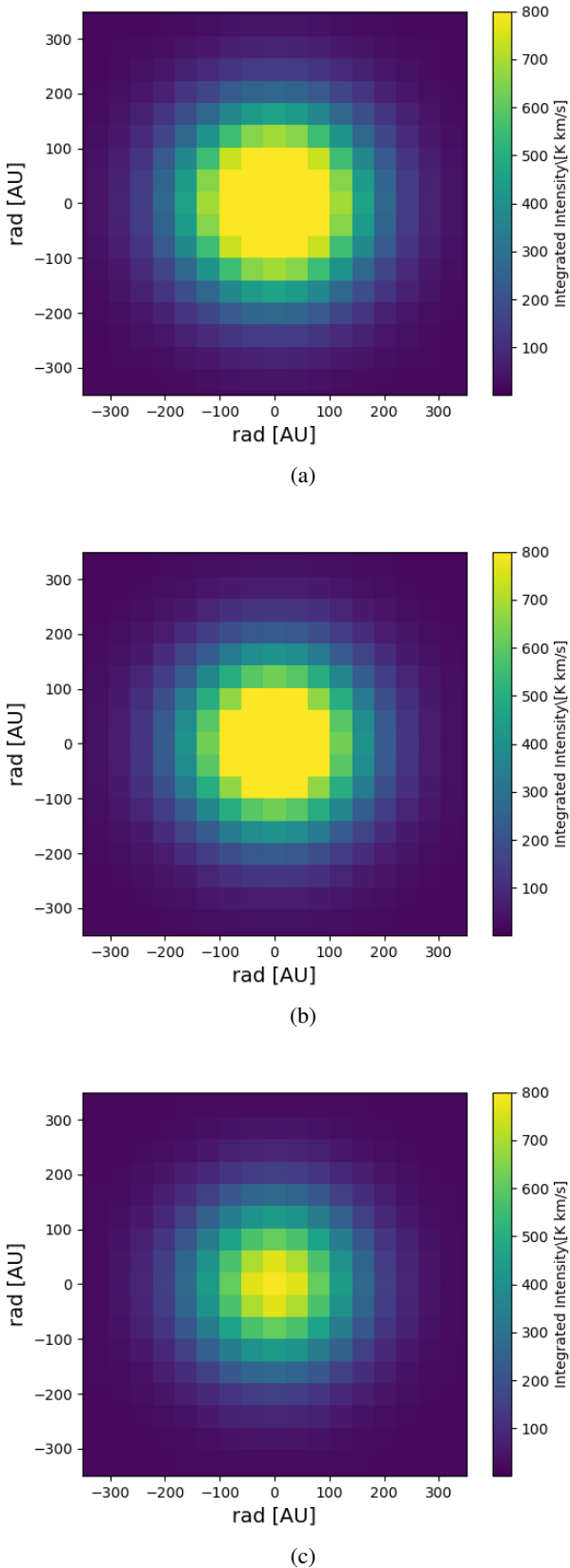
(a)

(b)

(c)

Fig. 5: Integrated intensity map of p-NH₃ (1,1) in the core for binding energy (a) 3870K (b) 4080K and (c) 5280K with envelope

data from Danby et al. (1988)) do not resolve the hyperfine

structure, and hence we assumed that the coefficients for the individual hyperfine components were distributed according to LTE. To investigate the potential effect of hyperfine-resolved collisional rate coefficients on our results, we ran another series of line simulations adopting instead the set of collisional rate coefficients presented recently by Loreau et al. (2023). The hyperfine-resolved radiative transition frequencies and Einstein A coefficients were derived from data in the CDMS (Endres et al. 2016). These two approaches led only to small differences in simulated lines, and in what follows we present the results of simulations carried out using the data originating in LAMDA.

In each model, we observe that the peak intensity is centrally concentrated and declines going outwards. The location and size of this zone are in good agreement with the simulations of the column densities (Fig. 4), despite optical thickness effects that were missed by calculating the column density directly from the simulated abundances. Predominantly, the intensity originates from the inner zone due to elevated NH₃ gas-phase abundance, as indicated by the abundance profiles (Fig. 2). Moreover, the size of the emitting region diminishes with higher binding energy, attributed to a reduction in gas-phase NH₃ concentrations associated with increasing binding energy. Similar results are obtained for radiative transfer models using the (2,2) and (3,3) lines.

Convolutions of the spectra for the (1,1) transitions at larger beam sizes are also conducted to evaluate the observability of this variation in the size of the emitting region. However, these effects become discernible only with beam sizes of 10 arcsec or smaller. This highlights the need for higher-resolution observations to detect such subtleties in the star-formation process. When convolved with a 6 arcsec beam, similar to in the observations by Mundy et al. (1990), we obtain brightness temperatures lower than but within a factor of two compared to their reported value of 16.5 K for the NH₃ (1,1) emission towards the brightest regions of their source - IRAS 16293-2422. They report NH₃ emissions arising from a ring-like region of 3000-4000 AU with a resolution of 6 arcsec (960 AU). In contrast, the BE-related effects in the model used in the present work originate from a region smaller than 300 AU, indicating that higher resolution observations will be necessary to draw important conclusions regarding effects due to NH₃ binding energy towards this source. Additionally, we ran radiative transfer models assuming higher velocity resolution (0.15 km/s) for the lines based on observations by Crapsi et al. (2007) using the Very Large Array (VLA) and found no difference in our results. Using the higher resolution requires more computational time but does not impact the results, so we decided to retain the lower velocity resolution for our models.

4. Discussion

4.1. Influence of NH₃ binding energy on abundance profiles of chemically related species

Interestingly, notable effects are observed on other species and their abundance profiles within the same zone where NH₃ abundances vary. A few examples are demonstrated in Fig. 3. The abundance profiles of these species vary depending on the chosen binding energy of NH₃. To understand this, let us consider the example of HNC (Fig. 6). In the inner regions of the model with binding energy = 3780K, HNC is efficiently pro-

duced through the reaction between HCNH$^+$ and NH$_3$, yielding HCN and HNC. HCNH$^+$ originates from HCN through the interaction with H$_3^+$ and can revert to HCN via reactions between HCNH$^+$ and H$_2$CO (and HCNH$^+$ + NH$_3$). Hence, the connection between HCN and HNC follows the sequence HCN → HCNH$^+$ → HNC, where the first step involves H$_3^+$, and the second step involves NH$_3$.

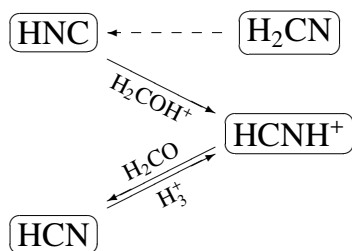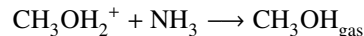### NH$_3$ binding energy = 3780 K
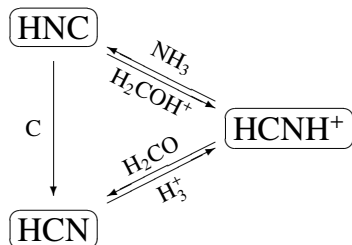
NH$_3$ binding energy = 5280 K

Fig. 6: Main formation and destruction pathways of HNC as predicted by the chemical model for the two extreme binding energy (BE) values. In the lower figure (BE = 5280 K), the dashed arrow represents an alternative pathway for the formation of HNC through H-abstraction from H$_2$CN. This pathway becomes prominent when the gas-phase abundance of NH$_3$ is low, thereby inhibiting the formation via the reaction between NH$_3$ and HCNH$^+$.

In contrast, in the model with binding energy = 5280K, the gas phase abundance of NH$_3$ is low, which effectively closes off the HCNH$^+$ + NH$_3$ route. HNC is being created instead via H-abstraction from H$_2$CN (dashed arrow in Fig. 6), but at approximately ~10% of the rate of the NH$_3$ route of the previous model; HNC formation is severely inhibited by the lack of available NH$_3$. This can be seen in Fig. 3 where the shape of the HNC abundance profile follows that of NH$_3$. Simultaneously, the rate of the reaction HCNH$^+$ + H$_2$CO → HCN + H$_2$COH$^+$ increases (as the HCNH$^+$ destruction channel with NH$_3$ is absent). These findings support the importance of further investigations into the role of NH$_3$ binding energy in the abundances of various species in the protostellar core.

4.2. Effect of Proton Transfer reactions on NH$_3$ abundances

Taquet et al. (2016) demonstrated that methanol abundances are significantly enhanced through proton transfer reactions involving NH$_3$, as compared to simulations lacking NH$_3$.

Subsequently, we introduced the following reaction

$$CH_3OH_2^+ + NH_3 \longrightarrow CH_3OH_{gas}$$

derived from the network outlined in their research, which contributes to the synthesis of dimethyl ether or methyl formate. We then ran a new chemical simulation with this reaction included, wherein only NH$_3$ binding energies were varied to investigate potential effects on methanol abundances. For this test, we used the KIDA network (Wakelam et al. 2015) in place of our full deuterium and spin-state containing networks, for two main reasons: 1) to check if our overall conclusions on the binding energy-dependent NH$_3$ desorption region remain unaffected regardless of the chemical network used (i.e., that the presence of deuterium and spin states does not affect the conclusions to a significant degree); and 2) to search for potential effects on some complex organic molecules (COMs) that are not included in our fiducial chemical network (for example, CH$_3$OCH$_3$, CH$_3$CH$_2$OH, etc). The grain-surface network used in this test is the same as our fiducial one, but with deuterium and spin states removed.

In the investigation of Taquet et al. (2016), protonation by NH$_3$ extended the survival time of methanol from 10^4 years to 10^5 years. In our study, methanol remained for up to 10^6 years even without their reaction integrated into the KIDA network. Upon inclusion of their reaction, our simulations validated their results, showing an increase in methanol abundances of up to two orders of magnitude for a specific binding energy value. However, this enhancement became noticeable only beyond 10^6 years. Analysis of abundances for different binding energy values at a specific time step revealed marginal variations in methanol abundances, even at 10^6 years, where the most substantial difference emerged between simulations with and without the proton-transfer reaction. The discrepancy in the evolutionary time in our model versus that of Taquet et al. (2016) regarding when the effect on CH$_3$OH becomes apparent is very likely due to different simulation parameters. We have not attempted to duplicate their results. Nevertheless, the comparison indicates that proton-transfer reactions can be very important and should be explored in more detail in later simulations.

5. Conclusions

NH$_3$ is an important molecule widely observed in various astronomical sources and on dust grain surfaces. However, uncertainties pertaining to its binding energy values prevent an accurate determination of its abundance and role in the chemistry of star and planet formation. The binding energy is a key parameter determining the abundance and chemistry of a species in the ISM. Recent studies have challenged previous notions of a unique binding energy value for NH$_3$ proposing instead a multi-binding energy approach.

Drawing on previously established experimental work by Kakkenpara Suresh et al. (2024), we incorporated multiple NH$_3$ binding energy values derived from these studies into gas-grain chemical networks to examine their impact on NH$_3$ abundance within a protostellar core. We conducted multiple simulations, systematically varying only the NH$_3$ binding energy, to discern its influence on the abundance profiles of NH$_3$ and other species. Our findings reveal a distinct dependence of NH$_3$ abundance

profiles on the binding energy employed, particularly in the inner warm regions of the model. This variability extends its influence on other key species, including HCN, HNC, CN, wherein the NH$_3$ abundance dictates the preferred pathway for their formation. On the contrary, in proton transfer reactions involving NH$_3$, expected to enhance methanol formation, the abundance variation of NH$_3$ due to binding energy does not appear to be a significant contributing factor.

Simulation of column density maps for p-NH$_3$ reveals that the size of the desorption region diminishes as the binding energy increases. These findings align with radiative transfer studies on the (1,1) inversion line of NH$_3$, where we added an envelope to our physical model to examine absorption and emission effects. In these studies, we observed that the peak intensity is centrally concentrated and decreases outward. Additionally, the intensity diminishes with higher binding energy due to a reduction in gas-phase NH$_3$. Our results highlight the importance of considering diverse binding energies in astrochemical models, providing a refined understanding of molecular cloud chemistry and star formation processes.

For future work, it is crucial to refine our understanding by further exploring the impact of varied binding energies on complex organic molecules (COMs) within astrochemical models. Additionally, investigations into the spatial distribution and temporal evolution of species influenced by multi-binding energy approaches would contribute valuable insights. The present results apply at very early times in the core evolution when the substructure is still absent and, hence, probe the very early stages of forming protostellar systems. Consequently, there is a critical need to enhance the physical model, incorporating more precise representations of observed substructures within protostellar cores. This improvement is essential for providing a more accurate and detailed description of the underlying phenomena in such sources.

References

Boogert, A. A., Gerakines, P. A., & Whittet, D. C. 2015a, Annual Review of Astronomy and Astrophysics, 53, 541

Boogert, A. A., Gerakines, P. A., & Whittet, D. C. 2015b, Annual Review of Astronomy and Astrophysics, 53, 541

Bovolenta, G., Bovino, S., Vöhringer-Martinez, E., et al. 2020, Molecular Astrophysics, 21, 100095

Brünken, S., Sipilä, O., Chambers, E. T., et al. 2014, Nature, 516, 219

Caselli, P., Pineda, J. E., Sipilä, O., et al. 2022, The Astrophysical Journal, 929, 13

Caselli, P., Walmsley, C., Tafalla, M., Dore, L., & Myers, P. 1999, The Astrophysical Journal, 523, L165

Cheung, A. C., Rank, D. M., Townes, C. H., Thornton, D. D., & Welch, W. J. 1968, Phys. Rev. Lett., 21, 1701

Crabtree, K. N., Indriolo, N., Kreckel, H., Tom, B. A., & McCall, B. J. 2011, The Astrophysical Journal, 729, 15

Crapsi, A., Caselli, P., Walmsley, M. C., & Tafalla, M. 2007, Astronomy & Astrophysics, 470, 221

Crimier, N., Ceccarelli, C., Maret, S., et al. 2010, Astronomy & Astrophysics, 519, A65

Danby, G., Flower, D. R., Valiron, P., Schilke, P., & Walmsley, C. M. 1988, MNRAS, 235, 229

Endres, C. P., Schlemmer, S., Schilke, P., Stutzki, J., & Müller, H. S. P. 2016, Journal of Molecular Spectroscopy, 327, 95

Fehér, O., Tóth, L. V., Kraus, A., et al. 2022, The Astrophysical Journal Supplement Series, 258, 17

Ferrero, S., Zamirri, L., Ceccarelli, C., et al. 2020, The Astrophysical Journal, 904, 11

Garrod, R. & Herbst, E. 2006, Astronomy & Astrophysics, 457, 927

Germain, A., Tinacci, L., Pantaleone, S., Ceccarelli, C., & Ugliengo, P. 2022, ACS Earth and Space Chemistry

Gorski, M., Ott, J., Rand, R., et al. 2018, The Astrophysical Journal, 856, 134

Grassi, T., Bovino, S., Caselli, P., et al. 2020, Astronomy & Astrophysics, 643, A155

Hama, T. & Watanabe, N. 2013, Chemical reviews, 113, 8783

Harju, J., Sipilä, O., Brünken, S., et al. 2017, The Astrophysical Journal, 840, 63

He, J., Acharyya, K., & Vidali, G. 2016, The Astrophysical Journal, 825, 89

Irvine, W., Goldsmith, P., Hjalmarson, Å., Hollenbach, D., & Thronson, H. 1987, Reidel Dordrecht, 561

Juvela, M. 2020, Astronomy & Astrophysics, 644, A151

Kakkenpara Suresh, S., Dulieu, F., Vitorino, J., & Caselli, P. 2024, Astronomy & Astrophysics, 682, A163

Keto, E. & Caselli, P. 2010, Monthly Notices of the Royal Astronomical Society, 402, 1625

Liszt, H., Lucas, R., & Pety, J. 2006, Astronomy & Astrophysics, 448, 253

Loreau, J., Faure, A., Lique, F., Demes, S., & Dagdigian, P. J. 2023, MNRAS, 526, 3213

Mundy, L. G., Wootten, H., & Wilking, B. A. 1990, Astrophysical Journal, Part 1 (ISSN 0004-637X), vol. 352, March 20, 1990, p. 159-166., 352, 159

Pagani, L., Bacmann, A., Cabrit, S., & Vastel, C. 2007, A&A, 467, 179

Penteado, E., Walsh, C., & Cuppen, H. 2017, The Astrophysical Journal, 844, 71

Poch, O., Istiqomah, I., Quirico, E., et al. 2020, Science, 367, eaaw7462

Salinas, V. N., Hogerheijde, M. R., Bergin, E. A., et al. 2016, Astronomy & Astrophysics, 591, A122

Sandqvist, A., Hjalmarson, Å., Frisk, U., et al. 2017, Astronomy & Astrophysics, 599, A135

Schöier, F. L., van der Tak, F. F. S., van Dishoeck, E. F., & Black, J. H. 2005, A&A, 432, 369

Sipilä, O. 2012, Astronomy & Astrophysics, 543, A38

Sipilä, O., Caselli, P., & Harju, J. 2015a, Astronomy & Astrophysics, 578, A55

Sipilä, O., Harju, J., Caselli, P., & Schlemmer, S. 2015b, Astronomy & Astrophysics, 581, A122

Sipilä, O., Hugo, E., Harju, J., et al. 2010, Astronomy & Astrophysics, 509, A98

Tafalla, M., Myers, P., Caselli, P., Walmsley, C., & Comito, C. 2002, The Astrophysical Journal, 569, 815

Taquet, V., Wirström, E. S., & Charnley, S. B. 2016, The Astrophysical Journal, 821, 46

Tinacci, L., Germain, A., Pantaleone, S., et al. 2022, ACS Earth and Space Chemistry, 6, 1514

Wakelam, V., Loison, J.-C., Herbst, E., et al. 2015, The Astrophysical Journal Supplement Series, 217, 20

Wakelam, V., Loison, J.-C., Mereau, R., & Ruaud, M. 2017, Molecular Astrophysics, 6, 22

Winnewisser, G., Churchwell, E., & Walmsley, C. 1979, Astronomy and Astrophysics, vol. 72, no. 1-2, Feb. 1979, p. 215-223., 72, 215

Appendix A: Relative Ice Abundances of Key Volatiles

In our model, low ice abundances in the central regions of the source, attributed to the high temperatures (approximately 200K), render these ice abundance values less meaningful. As a result, in Fig. A.1, we present simulated abundance ratios beyond 2000 AU only, where ice abundances are higher due to temperatures dropping to around 10-20 K. Our findings for CO and CH_3OH align well with the range observed in low-mass young stellar objects (LYSOs) as described in Boogert et al. (2015b). Although our estimates for CH_4 abundances are slightly elevated, they remain reasonably close to the values reported in the Boogert et al. (2015b). In our model, CO_2 exhibits levels lower by two orders of magnitude, while NH_3 is overestimated by a factor of three. These discrepancies may stem from a variety of factors, such as the elemental abundances used in our model, the impact of background emissions on the observed line intensities, or missing grain-surface chemistry (in the case of CO_2). A comprehensive discussion of the cause of these variations exceeds the scope of our current study and is therefore omitted.
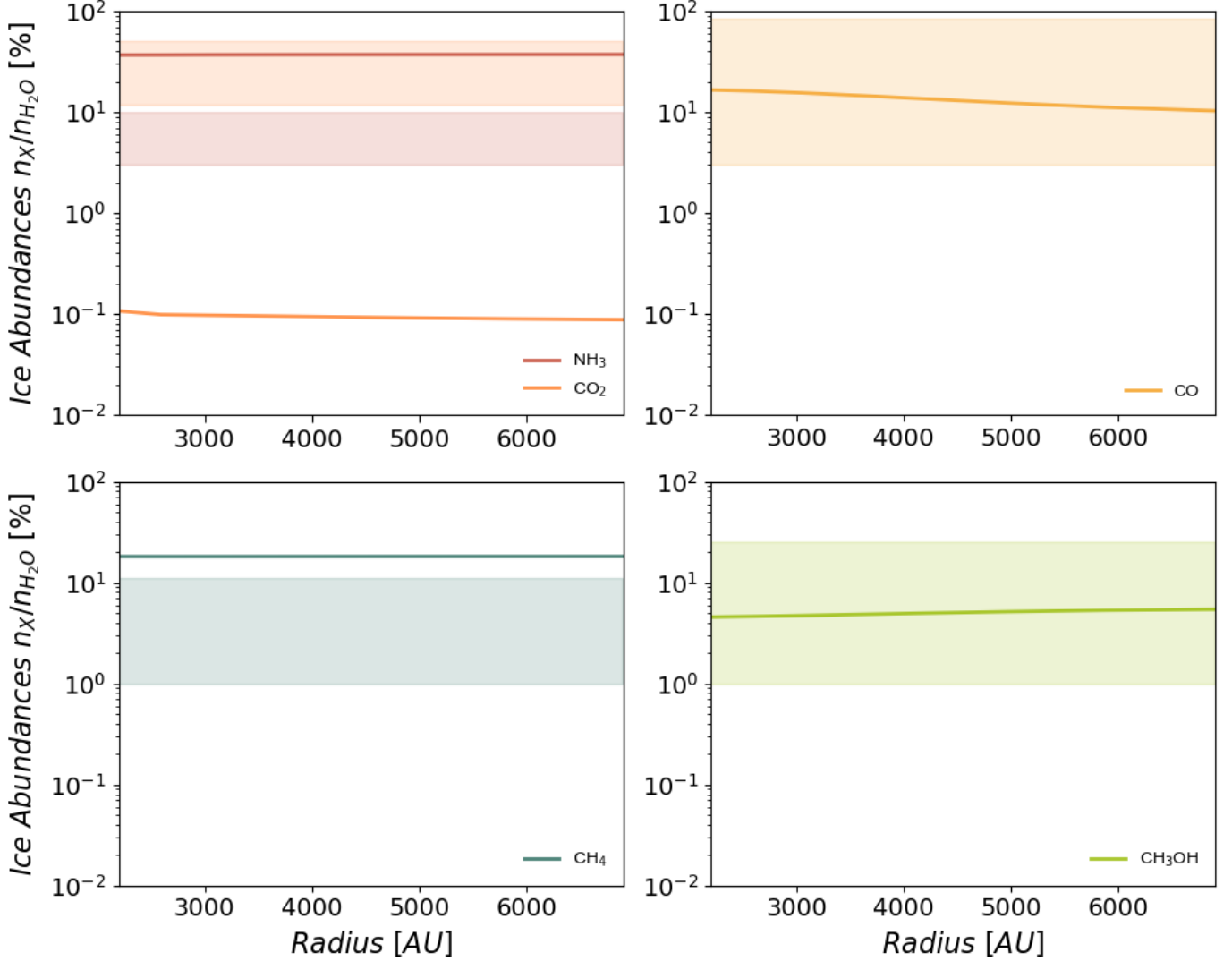

Fig. A.1: Relative ice abundances of key volatiles with respect to water ice. The solid lines represent values obtained in this work and the shaded zones of the same colour represent the range of observed values reported in Boogert et al. (2015b)